CRYSTAL GROWTH & DESIGN

pubs.acs.org/crystal

Article

A Phase-Field Model for Wet Snow Metamorphism

Published as part of Crystal Growth & Design special issue "Heterogeneous Drivers of Ice Formation".

Adrian Moure* and Xiaojing Fu*

Cite This: *Cryst. Growth Des.* 2024, 24, 7808−7821

Read Online

ACCESS | Metrics & More | Article Recommendations | Supporting Information

ABSTRACT: The microstructure of snow determines its fundamental properties such as mechanical strength, reflectivity, or thermo-hydraulic properties. Snow undergoes continuous microstructural changes due to local gradients in temperature, humidity, or curvature, in a process known as snow metamorphism. In this work, we focus on wet snow metamorphism, which occurs when the temperature is close to the melting point and involves phase transitions among liquid water, water vapor, and solid ice. We propose a pore-scale phase-field model that simultaneously captures the three relevant phase change phenomena: sublimation (deposition), evaporation (condensation), and melting (solidification). The phase-field formulation allows one to track the temperature evolution among the three phases and the water vapor concentration in the air. Our three-phase model recovers the corresponding two-phase transition model when one phase is not present in the system. 2D simulations of the model unveil the impact of humidity and temperature on the dynamics of wet snow metamorphism at the pore scale. We also explore the role of liquid melt content in controlling the dynamics of snow metamorphism in contrast to the dry regime before percolation onsets. The model can be readily extended to incorporate two-phase flow and may be the basis for investigating other problems involving water phase transitions in a vapor−solid−liquid system, such as airplane icing or thermal spray coating.

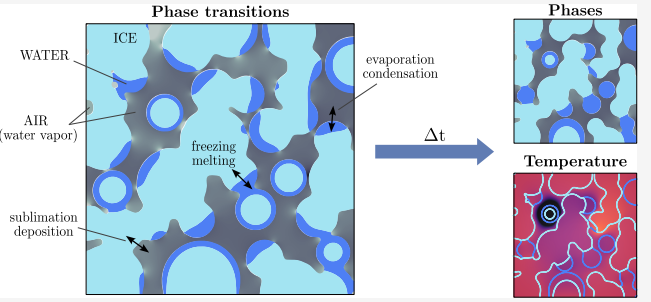

1. INTRODUCTION

Snow and firn are heterogeneous porous materials composed of two components, water and air, distributed among three phases: solid ice, liquid water, and air with water vapor. The microstructure of snow and firn dictates their mechanical strength, reflectivity, and thermo-hydraulic properties, which govern important processes such as snow avalanches, snowpack and glacial hydrology, radar remote sensing, and the performance of snow vehicles.[1] However, these properties constantly evolve because snow is a thermodynamically active material that undergoes continuous microstructural changes caused by phase transitions between ice, liquid water, and vapor, in a process known as snow metamorphism.[2] Ultimately, snow metamorphism leads to a denser snow consisting of coarser and rounder ice grains. Based on whether liquid water is present, snow metamorphism is considered to be of two types—dry and wet. Colbeck and other authors published a series of pioneer papers in the 1970s and 1980s[1−8] that derived the theoretical foundations to understand the mechanisms driving each type of snow metamorphism. Dry snow metamorphism[3,9] results from sublimation and deposition and is driven by the transport of water vapor between regions with different vapor pressures, i.e., regions with different temperatures and/or grain curvature, according to the Gibbs−Thomson condition.[10] On the other hand, wet snow metamorphism occurs when the temperature is close to the melting point. The presence of liquid water fundamentally alters the mechanisms of metamorphism by increasing the thermodynamic activity of snow and strengthening the mechanical and thermal connection between ice grains through capillary bridging.[1,3] Thus, compared to dry metamorphism, wet snow metamorphism displays accelerated coarsening and densification. Colbeck proposed two different regimes for wet metamorphism depending on the liquid water content (LWC): the pendular and the funicular regimes.[1] In the funicular regime, the LWC is high so that the water completely surrounds the ice grains. In the pendular regime, the LWC is low, and most of the ice surface is in contact with air. Thus, the pendular regime displays lower heat flow, grain growth, and snow densification and larger capillary forces and grain-to-grain mechanical strength, compared to the funicular regime. In both cases, vapor kinetics plays an important role.[2] While Colbeck's work provided a mechanistic understanding of snow meta-

Received: April 18, 2024
Revised: September 1, 2024
Accepted: September 3, 2024
Published: September 13, 2024

morphism, it focused on theoretical snow configurations under ideal environmental conditions. Subsequent experimental works used X-ray microtomography (microCT) to study the evolution of the dry snow microstructure in realistic scenarios under isothermal conditions[11,12] and temperature gradients.[13,14] Many authors leveraged the microCT data to perform a comprehensive analysis of local crystal growth laws[15,16] and validate mean field models.[17,18] The first experiments of wet metamorphism focused on fully saturated snow.[5] Improved experimental techniques enable studies of wet metamorphism on samples with a low LWC.[19−22] These works analyzed snow wetness and grain size and derived empirical laws for the snow properties under wet conditions.[23] However, more advanced techniques are still being developed to robustly visualize liquid water within snow samples, such as the use of hyperspectral imaging to map out the LWC in snow.[24]

Mathematical models may complement experimental development to provide insights into the metamorphism process. To this end, wet snow is modeled as a three-phase system composed of liquid water, vapor, and solid ice and thus can be grouped with other class problems such as snowflake growth and water drop icing in a humidity-controlled atmosphere. In this broader group of literature studies, some have proposed a simplified 1D model to describe the role of humidity in the evolution dynamics.[25] More elaborated 2D continuum models resorted to the phase-field method[26,27] or the level-set method,[28,29] which have been successful in reproducing the phase transitions between two phases of water, i.e., solidification,[30−32] sublimation,[33−35] and evaporation.[36−39] However, most of these continuum models are limited to the two-phase regime and do not simultaneously capture the transitions among the three water phases; thus, these models do not address the wet snow metamorphism problem.

Here, we propose a phase-field model that describes the nonequilibrium evolution of the three-phase mixture composed of liquid water, water vapor, and solid ice. The modeling choice is inspired by recent applications of phase-field methods in porous media problems with phase transitions, including the modeling of microstructural evolution of porous materials and multicomponent fluid mixtures,[34,40−44] phase transitions during two-phase flow in porous media,[45,46] and crystallization flow in porous media.[47−49] The three-phase model proposed in this work reduces to the classic two-phase model in the absence of a third phase, and the resulting two-phase models readily capture the Gibbs−Thomson conditions. The model allows us to analyze the pore-scale dynamics that dictate wet snow metamorphism. Currently, the model does not account for granular compaction, melt film imbibition, or melt percolation. Rather, the primary focus of the model is to elucidate the role of thermodynamically driven phase transitions in microstructure evolution of a quiescent wet snow mixture.

2. PHASE-FIELD MODEL FOR A WET SNOW MIXTURE

The phase-field method[50,51] is a mathematical technique that is based on a free energy description of multiphase mixtures and is well-suited for problems with moving interfaces. Within the phase-field framework, one defines a dimensionless *phase-field* variable, denoted as $\phi_l \in [0, 1]$, which represents the volume fraction of phase l at any given point in the domain. The phase variable smoothly transitions across the interface between two distinct phases (Figure 1). With the appropriate *evolution equations*, the moving boundary problem is reformulated in a fixed domain, which avoids most of the numerical issues caused by the moving interfaces.

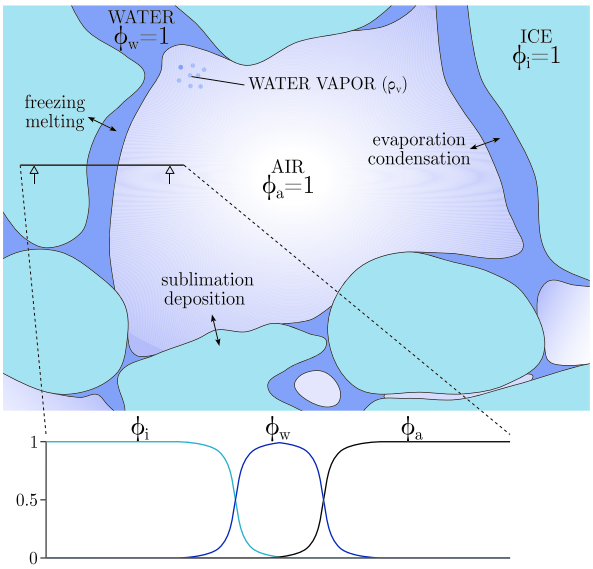

Figure 1. Illustration of the key model variables ϕ_a, ϕ_w, ϕ_i, and ρ_v as defined in the continuum domain composed of wet snow. The 1D transect profile illustrates the diffusive nature of the phase variables at the phase−phase boundaries. The model variable temperature T (not shown here) is also defined point-wise in the entire domain.

Here, we propose a *nonvariational* phase-field model that captures the phase transitions between ice, liquid water, and water vapor, i.e., solidification, sublimation, evaporation, and the opposite transitions. For simplicity, from here on, we denote liquid water as water and water vapor as vapor. We assume that the air is at atmospheric pressure. We assume that ice and water have an equal density for the phase evolution equations, which introduces a small mass conservation error. Although fluid flow is not considered in the current model, future work that incorporates fluid flow and unequal density may mitigate the mass conservation issue.

We note that in the spirit of numerical robustness and physical consistency, a *variational* phase-field formulation[52] is often more desirable to ensure non-negative entropy production and convergence toward equilibrium.[53,54] However, due to the close proximity in the density of the ice and liquid water phase, we find that formulating a free energy for the wet snow system based on the density field introduces numerical singularities in the formulation.

2.1. Model Variables. Our model unknowns are the phase-field variables for ice $\phi_i(\boldsymbol{x}, t)$, water $\phi_w(\boldsymbol{x}, t)$, and air $\phi_a(\boldsymbol{x}, t)$ phases (see Figure 1), as well as variables for temperature $T(\boldsymbol{x}, t)$ (units: °C) and vapor density $\rho_v(\boldsymbol{x}, t)$ (units: kg/m^3). All variables are defined point-wise in the problem domain Ω (Figure 1). Note that even though temperature and vapor density are not phase-field variables, here we leverage the formulation to specify phase-dependent temperature evolution (see Section 2.2.2) and localize the vapor dynamics onto the air phase (see Section 2.2.3).

2.2. Model Equations. In this section, we will introduce the five partial differential equations that describe the coevolution of our model variables.

https://doi.org/10.1021/acs.cgd.4c00539
Cryst. Growth Des. 2024, 24, 7808−7821

2.2.1. Phase Evolution Equations. The basic form of the phase evolution equations for the three phase-field variables is expressed as

$$\frac{\partial \phi_i}{\partial t} = -\frac{M_0}{\Sigma_i}\frac{\delta \mathcal{F}^{tri}(\bar{\phi})}{\delta \phi_i} - \alpha_{sol}\phi_i^2\phi_w^2\frac{T - T_{melt}}{L_{sol}/c_{p,w}} + \alpha_{sub}\phi_i^2\phi_a^2\frac{\rho_v - \rho_{vs}^I(T)}{\rho_i} + \theta_{nucl}(\bar{\phi}, T) \quad (1)$$

$$\frac{\partial \phi_w}{\partial t} = -\frac{M_0}{\Sigma_w}\frac{\delta \mathcal{F}^{tri}(\bar{\phi})}{\delta \phi_w} + \alpha_{sol}\phi_i^2\phi_w^2\frac{T - T_{melt}}{L_{sol}/c_{p,w}} + \alpha_{eva}\phi_w^2\phi_a^2\frac{\rho_v - \rho_{vs}^W(T)}{\rho_w} - \theta_{nucl}(\bar{\phi}, T) \quad (2)$$

$$\frac{\partial \phi_a}{\partial t} = -\frac{M_0}{\Sigma_a}\frac{\delta \mathcal{F}^{tri}(\bar{\phi})}{\delta \phi_a} - \alpha_{sub}\phi_i^2\phi_a^2\frac{\rho_v - \rho_{vs}^I(T)}{\rho_i} - \alpha_{eva}\phi_w^2\phi_a^2\frac{\rho_v - \rho_{vs}^W(T)}{\rho_w} \quad (3)$$

where $\delta \cdot /\delta \cdot$ denotes the variational derivative, and we use the notation $\bar{\phi} = \{\phi_i, \phi_w, \phi_a\}$. Note that eqs 1−3 account for total mass conservation by assuming an equal density of ice and water ($\rho_i = \rho_w$). The first terms on the right-hand side of these three equations capture the Allen−Cahn kinetics of phase-field variables,[55] where M_0 is the phase-dependent mobility defined below in Section 2.3 and $\mathcal{F}^{tri}$ is the classical energy functional of a ternary mixture:[51]

$$\mathcal{F}^{tri}(\bar{\phi}) = \int\left(\frac{3}{\varepsilon}F^{tri}(\bar{\phi}) + \frac{3}{2}\varepsilon[\Sigma_i(\nabla\phi_i)^2 + \Sigma_w(\nabla\phi_w)^2 + \Sigma_a(\nabla\phi_a)^2] + \beta(1 - \phi_i - \phi_w - \phi_a)\right)d\Omega \quad (4)$$

The parameter ε represents the width of the phase-field interface and β is the Lagrange multiplier (see Section 3). The function F^{tri} is the *triple-well potential*, defined as

$$F^{tri}(\bar{\phi}) = \frac{1}{2}\Sigma_i\phi_i^2(1 - \phi_i)^2 + \frac{1}{2}\Sigma_w\phi_w^2(1 - \phi_w)^2 + \frac{1}{2}\Sigma_a\phi_a^2(1 - \phi_a)^2 + \Lambda\phi_i^2\phi_w^2\phi_a^2 \quad (5)$$

where the Λ-term improves the dynamic consistency of the model[51] to mitigate the spurious effect along phase−phase boundaries. The parameters Σ_i, Σ_w, and Σ_a are related to the surface tensions (σ_{lm}) between phases l and m such that

$$\Sigma_i = \sigma_{iw} + \sigma_{ia} - \sigma_{wa}, \quad \Sigma_w = \sigma_{iw} + \sigma_{wa} - \sigma_{ia}, \quad \Sigma_a = \sigma_{wa} + \sigma_{ia} - \sigma_{iw} \quad (6)$$

We extend the Allen−Cahn kinetics with the α-terms in eqs 1−3, which account for the different phase transitions. In particular, the α_{sol} term accounts for solidification or melting, the α_{sub} term accounts for sublimation or deposition, and the α_{eva} term accounts for evaporation or condensation. The estimation of α's parameter values is described in the Supporting Information (Section 1 and Table S1). The parameters L_{sol}, $c_{p,w}$, ρ_w, and ρ_i are the solidification latent heat, water specific heat capacity, water density, and ice density, respectively. We follow Kaempfer and Plapp[34] and express the saturated vapor density of ice (ρ_{vs}^I) and water (ρ_{vs}^W) as

$$\rho_{vs}^J(T) = \rho_a 0.62\frac{P_{vs}^J(T)}{P_a - P_{vs}^J(T)} \quad (7)$$

where the index J stands for I and W, ρ_a is the dry air density, P_a is the atmospheric pressure (units: Pa), and P_{vs}^J is the saturated vapor pressure of phase J (units: Pa). The saturated vapor pressure of ice and water is defined as[56,57]

$$P_{vs}^I(T) = \exp\left(\sum_{j=0}^{4} k_j(T + T_0)^{j-1} + k_5\ln(T + T_0)\right) \quad (8)$$

$$P_{vs}^W(T) = \exp\left(\sum_{j=0}^{6} g_j(T + T_0)^{j-2} + g_7\ln(T + T_0)\right) \quad (9)$$

respectively, where T_0 = 273.15 °C, and the values of the parameters k_j and g_j are listed in Table S2 in the Supporting Information.

The θ_{nucl} terms in eqs 1 and 2 account for ice and water nucleation, which are necessary in order to trigger the nucleation of a third phase when only two phases exist initially. In particular, here we account for the nucleation of water when T increases above T_{melt} in an ice−air system and the nucleation of ice when T decreases below ice nucleation temperature T_{nucl} in a water−air system. We propose a phenomenological nucleation term

$$\theta_{nucl}(\bar{\phi}, T) = \alpha_{nucl}M_0\phi_a^2[\phi_w^2N_i(T) - \phi_i^2N_w(T)] \quad (10)$$

where α_{nucl} is a parameter controlling the strength of nucleation, and the ice and water nucleation functions $N_i(T)$ and $N_w(T)$, respectively, are expressed as

$$N_i(T) = 0.5 - 0.5\tanh[20(T - T_{nucl} + 0.1)], \quad N_w(T) = 0.5 + 0.5\tanh[20(T - T_{melt} - 0.1)] \quad (11)$$

Note that N_i becomes active when $T < T_{nucl}$, which allows the presence of undercooled water in the range $T_{nucl} < T < T_{melt}$. According to eq 10, ice nucleation occurs at the water−air interface when $T < T_{nucl}$ (note the term $\phi_a^2\phi_w^2$ multiplying N_i). Once ice nucleation advances, the water−air interface splits into water−ice and ice−air interfaces, resulting in $\phi_a^2\phi_w^2 = 0$ and thus θ_{nucl} stays zero even if $T < T_{nucl}$. Water nucleation exhibits analogous behavior. Note that θ_{nucl} only needs to be active until the system enters into the spinodal decomposition region of the ternary mixture.

2.2.2. Energy Conservation Equation. Here, we formulate conservation of energy in terms of temperature, expressed as

$$\rho(\bar{\phi})c_p(\bar{\phi})\frac{\partial T}{\partial t} = \nabla\cdot[K(\bar{\phi})\nabla T] + \rho(\bar{\phi})L_{sol}\left(\frac{\partial \phi_a}{\partial t} + \frac{\partial \phi_i}{\partial t}\right) - \rho(\bar{\phi})L_{sub}\frac{\partial \phi_a}{\partial t} \quad (12)$$

Equation 12 accounts for thermal diffusion and the latent heat released and/or absorbed during the different phase transitions. L_{sub} is the sublimation latent heat. The latent heat of evaporation is then captured through $L_{eva} = L_{sub} - L_{sol}$. The phase-dependent density (ρ), specific heat capacity (c_p), and thermal conductivity (K) are defined as

https://doi.org/10.1021/acs.cgd.4c00539
Cryst. Growth Des. 2024, 24, 7808−7821

$$\rho(\bar{\phi}) = \sum_{l=\mathrm{i,w,a}} \phi_l \rho_l;$$
$$c_p(\bar{\phi}) = \sum_{l=\mathrm{i,w,a}} \phi_l c_{p,l};$$
$$K(\bar{\phi}) = \sum_{l=\mathrm{i,w,a}} \phi_l K_l \tag{13}$$

where ρ_l, $c_{p,l}$, and K_l are the density, specific heat capacity, and thermal conductivity, respectively, of phase l. We assume that ρ_l, $c_{p,l}$, and K_l are constant in time. Note that here we violate our primary assumption that $\rho_\mathrm{i} = \rho_\mathrm{w}$ used in eqs 1−3, which incurs mass conservation error; instead, we consider different densities for the ice and water phases for the energy equation in order to adopt the correct heat capacity for each phase. Although doing so does not eliminate errors in energy conservation due to errors in mass conservation, it improves the thermal consistency of the model.

2.2.3. Mass Conservation of Vapor. The vapor mass conservation equation is expressed as

$$\frac{\partial(\phi_\mathrm{a}\rho_\mathrm{v})}{\partial t} = \nabla\cdot[\phi_\mathrm{a} D_\mathrm{v}(T)\nabla\rho_\mathrm{v}] + \rho_\mathrm{SE}\frac{\partial\phi_\mathrm{a}}{\partial t} \tag{14}$$

which accounts for vapor diffusion in the air and mass transfer of water during sublimation and evaporation (and the opposite transitions). Here, we formulate a phase-dependent density $\rho_\mathrm{SE}(\bar{\phi})$ such that $\rho_\mathrm{SE} = \rho_\mathrm{i}$ in the case of sublimation and $\rho_\mathrm{SE} = \rho_\mathrm{w}$ in the case of evaporation. The specific form for $\rho_\mathrm{SE}(\bar{\phi})$ is discussed and provided in eq 17 of Section 2.3. D_v is the vapor diffusion coefficient, whose dependence on T (in °C) follows the expression[58]

$$D_\mathrm{v}(T) = D_{\mathrm{v}0}\left(\frac{T + T_0}{T_0}\right)^{1.81} \tag{15}$$

where $D_{\mathrm{v}0}$ is the vapor diffusion coefficient at the freezing point and $T_0 = 273.15$.

2.3. Phase-Dependent Functions. The model equations introduced above rely on a few parameters that are phase-dependent. For material property parameters such as ρ, c_p, and K, we simply use phase-weighted averages as shown in eq 13. However, parameters such as the mobility function M_0 in eqs 1−3 and ρ_SE in eq 14 are related to phase change dynamics at phase−phase boundaries or triple junction regions and thus require more careful mathematical formulation. Here, we resort to the ternary diagram to illustrate these modeling choices.

A ternary diagram is a common tool to represent three-phase systems. In a ternary diagram, the vertex l represents the point $\phi_l = 1$, while the opposite side of that vertex represents the points $\phi_l = 0$ (for $l = \{\mathrm{i, w, a}\}$). The interior of the diagram represents points where the three phases coexist. Thus, any valid $\{\phi_\mathrm{i}, \phi_\mathrm{w}, \text{and } \phi_\mathrm{a}\}$ configuration is represented by a point in the ternary diagram. In particular, evaporation takes place on the side $\phi_\mathrm{i} = 0$, sublimation on the side $\phi_\mathrm{w} = 0$, and solidification on the side $\phi_\mathrm{a} = 0$.

At the boundaries of the ternary diagram (i.e., $\phi_\mathrm{a} = 0$, $\phi_\mathrm{w} = 0$, and $\phi_\mathrm{i} = 0$), the mobility function M_0 must take the values M_sol, M_sub, and M_eva that correspond to the kinetics of solidification, sublimation, and evaporation, respectively. The exact expressions for these parameters are provided in eqs (4), (9), and (10) of the Supporting Information. Within the interior region of the ternary diagram, however, M_0 needs to be interpolated based on M_sol, M_sub, and M_eva. A common choice is the cubic interpolation, which presents issues for two reasons:[59,60] (1) the triple junction is a region, not a point, where the three phases coexist; (2) the values of M_sol, M_sub, and M_eva range several orders of magnitude in this region (see Table S1 in the Supporting Information). Thus, a cubic interpolation of M_0 would result in large gradients in mobility within the interior of the ternary diagram, leading to severe numerical challenges. In addition, a nonunique value of M_0 within the triple junction is not physically consistent and results in unrealistic behavior of the triple junction.

To avoid these two issues, we propose a piecewise constant interpolation of M_0, similar to that proposed in Miyoshi and Takaki,[59] where M_0 takes a constant value near each of the three sides and in the interior region of the ternary diagram:

$$M_0(\bar{\phi}) = \begin{cases} M_\mathrm{sol} & \text{if } \phi_\mathrm{a} \le \phi_\mathrm{i},\ \phi_\mathrm{a} \le \phi_\mathrm{w},\ \text{and } \phi_\mathrm{a} < 0.01 \\ M_\mathrm{eva} & \text{if } \phi_\mathrm{i} < \phi_\mathrm{a},\ \phi_\mathrm{i} \le \phi_\mathrm{w},\ \text{and } \phi_\mathrm{i} < 0.01 \\ M_\mathrm{sub} & \text{if } \phi_\mathrm{w} < \phi_\mathrm{a},\ \phi_\mathrm{w} < \phi_\mathrm{i},\ \text{and } \phi_\mathrm{w} < 0.01 \\ M_\mathrm{av} & \text{otherwise} \end{cases} \tag{16}$$

where we take M_av as the geometric mean (i.e., $M_\mathrm{av} = \sqrt[3]{M_\mathrm{sub}M_\mathrm{sol}M_\mathrm{eva}}$). We find that eq 16, compared to a cubic interpolation, improves the numerical efficiency and allows us to simulate triple junctions while respecting the actual kinetics of the different phase transitions.

The density ρ_SE must take the value ρ_i in the case of sublimation and ρ_w in the case of evaporation (i.e., $\phi_\mathrm{w} = 0$ and $\phi_\mathrm{i} = 0$, respectively, in the ternary diagram). The value of ρ_SE along the side $\phi_\mathrm{a} = 0$ is irrelevant because $\rho_\mathrm{SE}\frac{\partial\phi_\mathrm{a}}{\partial t}$ (see eq 14) is zero on that side. We propose a cubic interpolation between the sides $\phi_\mathrm{w} = 0$ and $\phi_\mathrm{i} = 0$ in the ternary diagram such that the derivatives of $\rho_\mathrm{SE}(\bar{\phi})$ are zero on the sides $\phi_\mathrm{w} = 0$ and $\phi_\mathrm{i} = 0$. We define the function ρ_SE as

$$\rho_\mathrm{SE}(\bar{\phi}) = \begin{cases} \dfrac{\rho_\mathrm{i} + \rho_\mathrm{w}}{2} + \dfrac{\rho_\mathrm{w} - \rho_\mathrm{i}}{4} x_\mathrm{SE}(3 - x_\mathrm{SE}^2) & \text{if } \phi_\mathrm{a} \ne 1 \\ \dfrac{\rho_\mathrm{i} + \rho_\mathrm{w}}{2} & \text{if } \phi_\mathrm{a} = 1 \end{cases}$$
$$\text{with } x_\mathrm{SE} = \frac{1 - \phi_\mathrm{a} - 2\phi_\mathrm{i}}{1 - \phi_\mathrm{a}} \tag{17}$$

Equation 17 displays a discontinuity at $\phi_\mathrm{a} = 1$. From a physical and numerical point of view, this discontinuity does not represent an issue because the term $\rho_\mathrm{SE}\frac{\partial\phi_\mathrm{a}}{\partial t}$ is zero if $\phi_\mathrm{a} = 1$. Nevertheless, we implement a regularization of eq 17 (see Section 2.5 in the Supporting Information).

2.4. Gibbs−Thomson Condition. The Gibbs−Thomson effect describes the deviations in the equilibrium chemical potential at a two-phase boundary due to the curvature of the interface. Such an effect readily applies to the three types of interfaces considered in wet snow and influences both the kinetics and equilibrium conditions experienced by curved interfaces. In Section 1 of the Supporting Information, we show that our model is equivalent to the two-phase models for solidification, sublimation, and evaporation when only two phases are present, and the resulting reduced model equations recover the Gibbs−Thomson condition for two-phase boundaries under certain conditions. In particular, our model reproduces, under certain parameter regimes, the kinetics

https://doi.org/10.1021/acs.cgd.4c00539
Cryst. Growth Des. 2024, 24, 7808−7821

defined by the Gibbs–Thomson condition for ice–liquid interfaces:

$$\frac{T - T_{\mathrm{melt}}}{L_{\mathrm{sol}}/c_{p,\mathrm{w}}} = -d_{\mathrm{sol}}\chi - \beta_{\mathrm{sol}}v_{\mathrm{n}} \tag{18}$$

where T is the interface temperature, β_{sol} is the kinetic attachment coefficient, d_{sol} is the capillary length, χ is the curvature of the interface (positive for spherical ice grains), and v_{n} is the normal velocity of the interface (positive for ice growth). Note that, at thermodynamic equilibrium (i.e., $v_{\mathrm{n}} = 0$), eq 18 simplifies to the classic Gibbs–Thomson equation:

$$T^{\mathrm{equil}} = T_{\mathrm{melt}} - \frac{L_{\mathrm{sol}}d_{\mathrm{sol}}}{c_{p,\mathrm{w}}}\chi \tag{19}$$

which states that the actual equilibrium temperature for solidification is lower than $T_{\mathrm{melt}} = 0$ °C for spherical ice grains. Similarly, our model captures, under certain parameter regimes, the kinetics defined by the Gibbs–Thomson condition for air–ice interfaces:

$$\frac{\rho_{\mathrm{v}} - \rho_{\mathrm{vs}}^{\mathrm{I}}(T)}{\rho_{\mathrm{vs}}^{\mathrm{I}}(T)} = d_{\mathrm{sub}}\chi + \beta_{\mathrm{sub}}v_{\mathrm{n}} \tag{20}$$

and for air–liquid interfaces:

$$\frac{\rho_{\mathrm{v}} - \rho_{\mathrm{vs}}^{\mathrm{W}}(T)}{\rho_{\mathrm{vs}}^{\mathrm{W}}(T)} = d_{\mathrm{eva}}\chi + \beta_{\mathrm{eva}}v_{\mathrm{n}} \tag{21}$$

where β_{sub} and d_{sub} are the Gibbs–Thomson coefficients for sublimation and β_{eva} and d_{eva} are the Gibbs–Thomson coefficients for evaporation. The model's versatility in capturing the Gibbs–Thomson conditions for all three types of two-phase boundaries relies on the phase-dependent formulation of M_0 as discussed in Section 2.3.

Note that because we do not assume equal Σ_α's, a spurious phase (nonphysical third phase) may appear along phase–phase boundaries, leading to inaccuracies in the equilibrium interface solution. We mitigate this issue using the Λ-term in the free energy formulation (eq 5). In addition, we note that the Gibbs–Thomson condition is only recovered in phase-field models under certain parameter conditions[34] or mathematical constructions through asymptotic analysis.[53,61,62] Our current formulation does not entail the mathematical additions needed to recover the Gibbs–Thomson condition for all interfaces for all parameter regimes; however, under certain parameter regimes, the model recovers these conditions. More details are provided in Section 3.2 and Supporting Information.

3. NUMERICAL IMPLEMENTATION

We first apply the phase constraint $\phi_{\mathrm{w}} = 1 - \phi_{\mathrm{i}} - \phi_{\mathrm{a}}$ to eqs 1–3, which allows us to compute the Lagrange multiplier β in eq 4 and eliminate one phase evolution equation:

$$\beta = \frac{1}{\frac{1}{\Sigma_{\mathrm{a}}} + \frac{1}{\Sigma_{\mathrm{w}}} + \frac{1}{\Sigma_{\mathrm{i}}}} \frac{3}{\varepsilon}\left(\frac{1}{\Sigma_{\mathrm{i}}}\frac{\partial F^{\mathrm{tri}}}{\partial \phi_{\mathrm{i}}} + \frac{1}{\Sigma_{\mathrm{w}}}\frac{\partial F^{\mathrm{tri}}}{\partial \phi_{\mathrm{w}}} + \frac{1}{\Sigma_{\mathrm{a}}}\frac{\partial F^{\mathrm{tri}}}{\partial \phi_{\mathrm{a}}}\right) \tag{22}$$

The resulting system of four coupled partial differential equations are

$$\begin{aligned}\frac{\partial \phi_{\mathrm{i}}}{\partial t} = &-\frac{3M_0(\bar{\phi})}{\varepsilon\Sigma_T}\left[(\Sigma_{\mathrm{w}} + \Sigma_{\mathrm{a}})\frac{\partial F^{\mathrm{tri}}}{\partial \phi_{\mathrm{i}}} - \Sigma_{\mathrm{a}}\frac{\partial F^{\mathrm{tri}}}{\partial \phi_{\mathrm{w}}} - \Sigma_{\mathrm{w}}\frac{\partial F^{\mathrm{tri}}}{\partial \phi_{\mathrm{a}}}\right] \\ &+ 3M_0(\bar{\phi})\varepsilon\nabla^2\phi_{\mathrm{i}} - \alpha_{\mathrm{sol}}\phi_{\mathrm{i}}^2\phi_{\mathrm{w}}^2\frac{T - T_{\mathrm{melt}}}{L_{\mathrm{sol}}/c_{\mathrm{p,w}}} \\ &+ \alpha_{\mathrm{sub}}\phi_{\mathrm{i}}^2\phi_{\mathrm{a}}^2\frac{\rho_{\mathrm{v}} - \rho_{\mathrm{vs}}^{\mathrm{I}}(T)}{\rho_{\mathrm{i}}} + \alpha_{\mathrm{nucl}}M_0(\bar{\phi})\phi_{\mathrm{a}}^2 \\ &[\phi_{\mathrm{w}}^2 N_{\mathrm{i}}(T) - \phi_{\mathrm{i}}^2 N_{\mathrm{w}}(T)]\end{aligned} \tag{23}$$

$$\begin{aligned}\frac{\partial \phi_{\mathrm{a}}}{\partial t} = &-\frac{3M_0(\bar{\phi})}{\varepsilon\Sigma_T}\left[-\Sigma_{\mathrm{w}}\frac{\partial F^{\mathrm{tri}}}{\partial \phi_{\mathrm{i}}} - \Sigma_{\mathrm{i}}\frac{\partial F^{\mathrm{tri}}}{\partial \phi_{\mathrm{w}}} + (\Sigma_{\mathrm{i}} + \Sigma_{\mathrm{w}})\right. \\ &\left.\frac{\partial F^{\mathrm{tri}}}{\partial \phi_{\mathrm{a}}}\right] + 3M_0(\bar{\phi})\varepsilon\nabla^2\phi_{\mathrm{a}} - \alpha_{\mathrm{sub}}\phi_{\mathrm{i}}^2\phi_{\mathrm{a}}^2\frac{\rho_{\mathrm{v}} - \rho_{\mathrm{vs}}^{\mathrm{I}}(T)}{\rho_{\mathrm{i}}} \\ &- \alpha_{\mathrm{eva}}\phi_{\mathrm{w}}^2\phi_{\mathrm{a}}^2\frac{\rho_{\mathrm{v}} - \rho_{\mathrm{vs}}^{\mathrm{W}}(T)}{\rho_{\mathrm{w}}}\end{aligned} \tag{24}$$

$$\begin{aligned}\frac{1}{\xi_{\mathrm{T}}}\rho(\bar{\phi})c_p(\bar{\phi})\frac{\partial T}{\partial t} = &\nabla\cdot[K(\bar{\phi})\nabla T] + \rho(\bar{\phi}) \\ &L_{\mathrm{sol}}\left(\frac{\partial \phi_{\mathrm{a}}}{\partial t} + \frac{\partial \phi_{\mathrm{i}}}{\partial t}\right) - \rho(\bar{\phi})L_{\mathrm{sub}}\frac{\partial \phi_{\mathrm{a}}}{\partial t}\end{aligned} \tag{25}$$

$$\frac{1}{\xi_{\mathrm{v}}}\frac{\partial(\phi_{\mathrm{a}}\rho_{\mathrm{v}})}{\partial t} = \nabla\cdot[\phi_{\mathrm{a}}D_{\mathrm{v}}(T)\nabla\rho_{\mathrm{v}}] + \rho_{\mathrm{SE}}(\bar{\phi})\frac{\partial \phi_{\mathrm{a}}}{\partial t} \tag{26}$$

where F^{tri}, ρ_{SE}, and M_0 are defined in eqs 5, 17, and 16, respectively. The saturated vapor densities $\rho_{\mathrm{vs}}^{\mathrm{I}}$ and $\rho_{\mathrm{vs}}^{\mathrm{W}}$ are defined in eqs 7–9. The parameter $\Sigma_{\mathrm{T}} = \Sigma_{\mathrm{i}}\Sigma_{\mathrm{w}} + \Sigma_{\mathrm{i}}\Sigma_{\mathrm{a}} + \Sigma_{\mathrm{w}}\Sigma_{\mathrm{a}}$, where Σ_l's are defined in eq 6. The nucleation functions N_{i} and N_{w} are defined in eq 11. The phase-dependent functions ρ, c_p, and K are defined through eq 13, and D_{v} follows eq 15. The time scaling parameters ξ_{T} and ξ_{v} are introduced in the next section (Section 3.1). The rest of the model parameters are listed in Tables S1 and S3 in the Supporting Information.

3.1. Temporal Scaling. Wet snow metamorphism involves multiple coupled processes on different time scales. Assuming a characteristic length scale of $L = 10^{-4}$ m, the characteristic times for different processes can range from $\sim 10^{-4}$ s for vapor diffusion to $\sim 10^{4}$ s for sublimation (see Section 2.1 in the Supporting Information for detailed calculations). A monolithic numerical solver requires the use of time steps that resolve the fastest process (i.e., vapor diffusion at $\sim 10^{-4}$ s), which would significantly increase the computational cost. Here, we leverage the procedure explained in Kaempfer and Plapp[34] to speed up the simulations. This approach leverages the fact that T and ρ_{v} are quasi-steady compared to the phase transition kinetics. The procedure consists of multiplying the right-hand side of the T and ρ_{v} equations (eqs 12 and 14, respectively) by a time-scale factor (ξ_{T} and ξ_{v} respectively) so that the process of vapor and thermal diffusion is numerically slowed down by orders of magnitude while still maintaining a quasi-steady state in T and ρ_{v}. This approach enables the use of longer time steps without introducing noticeable errors in the simulations. In this work, we take $\xi_{\mathrm{v}} = 10^{-3}$ and $\xi_{\mathrm{T}} = 1$ or $\xi_{\mathrm{T}} = 10^{-2}$ depending on whether or not solidification occurs in any parts of the domain. More details on this procedure are described in Section 2.1 of the Supporting Information.

https://doi.org/10.1021/acs.cgd.4c00539
Cryst. Growth Des. 2024, 24, 7808–7821

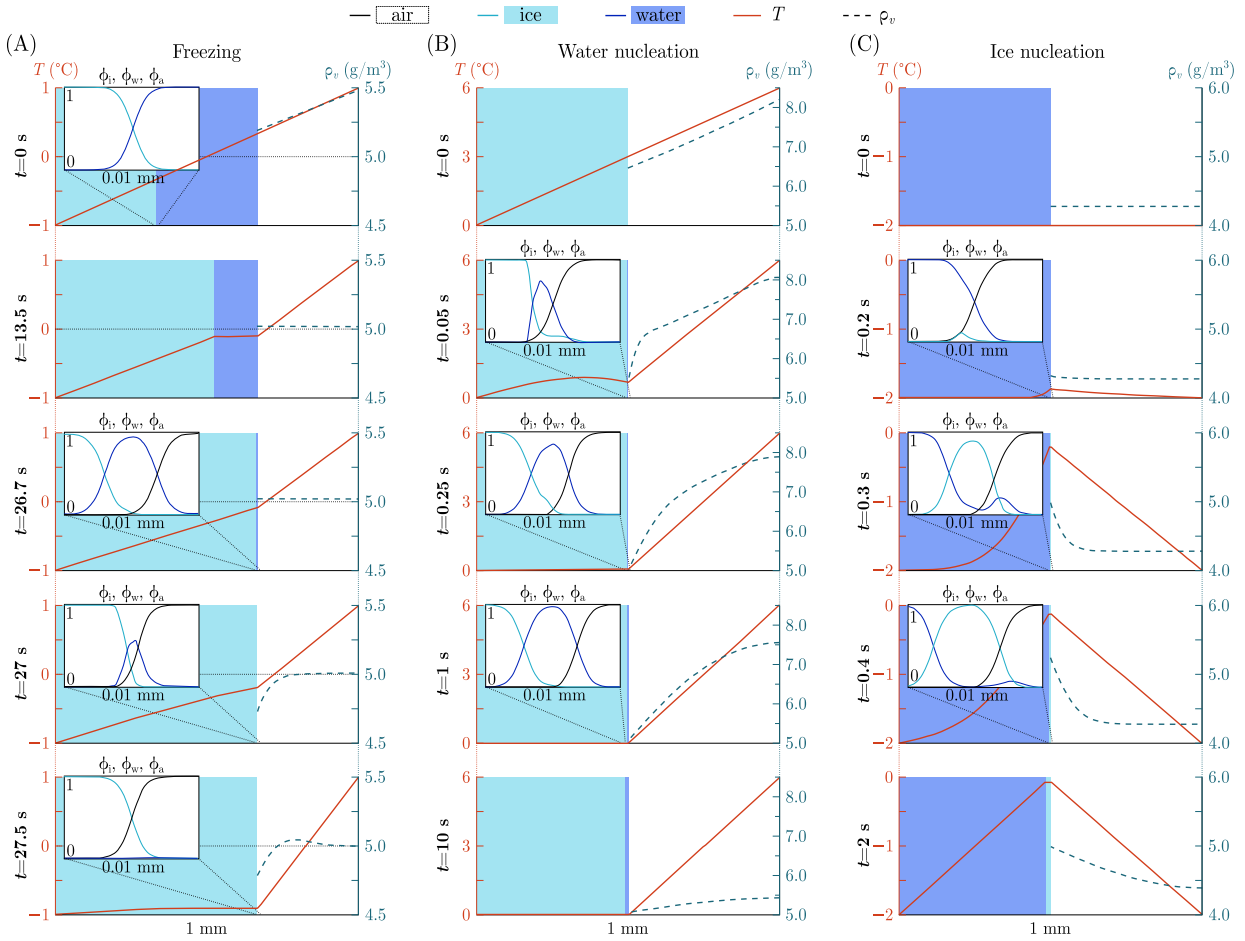

Figure 2. Time evolution (from top to bottom) of (A) directional water freezing toward the vapor phase, (B) water nucleation during melting of an initially dry system, and (C) ice nucleation during an initially ice-free system. The shaded regions in the main panels represent the different phases (light blue, dark blue, and unshaded for ice, water, and air, respectively). The red solid line indicates the temperature (left axis) and the dashed blue line indicates the vapor density in the air (right axis). The insets show the diffusive profiles of ϕ_i (light blue), ϕ_w (dark blue), and ϕ_a (black) around the interface where a phase change is occurring.

3.2. Kinetic Parameter Constraints. In order to accurately capture the interface kinetics set by the Gibbs–Thomson conditions, certain model parameters must be constrained by the interface physics. To this end, the relations between the Gibbs–Thomson parameters (β_j, d_j) and our model parameters (M_j, α_j) (for $j = \{\text{sol,sub,eva}\}$; see Section 1 in the Supporting Information) can be formulated from asymptotic analysis[32,61] but are only valid under certain conditions. In particular, we note that these asymptotic analyses do not readily apply to the wet snow problem as they were originally developed for compositional problems with symmetric[32,61] and asymmetric diffusivities.[62,63] Solutions using antitrapping current have been devised for the thermal problems but only with symmetric diffusivities.[53] Thus, in order to robustly capture the Gibbs–Thomson condition under all parameter regimes for the wet snow problem, further mathematical additions remain to be developed.

We note, however, in the earlier and similar work on dry snow metamorphism by Kaempfer and Plapp[34] that if we impose $\varepsilon < D\beta'$, where D are the different thermal or vapor diffusivities and β' is the scaled kinetic coefficient, then no antitrapping current is needed to correctly recover the sharp-interface limit. In particular, for the wet snow problem, this corresponds to the following sets of constraints:

$$\varepsilon < \beta_{\text{sol}} \frac{K_w}{\rho_w c_{p,w}} \approx 10^{-5}\ \text{m} \quad \text{(for water–ice interface)} \tag{27}$$

$$\varepsilon < \beta_{\text{sub}} \frac{\rho_{vs}}{\rho_i} \frac{K_a}{\rho_a c_{p,a}} \approx 10^{-7}\ \text{m} \quad \text{(for air–ice interface)} \tag{28}$$

$$\varepsilon < \beta_{\text{eva}} \frac{\rho_{vs}}{\rho_i} \frac{K_w}{\rho_w c_{p,w}} \approx 10^{-8}\ \text{m} \quad \text{(for air–water interface)} \tag{29}$$

These conditions impose a restriction on ε, which represents the diffusive interface width at phase–phase boundaries. The value of ε dictates the spatial discretization of our model, which must be fine enough to resolve the interface width with sufficient numerical elements. Given that the most restrictive conditions of the above require $\varepsilon < 10^{-8}$ m, this severely restricts the domain size we can simulate. In order to speed up the simulations, we consider a value $\varepsilon < 10^{-6}$ m, which allows us to use a coarser spatial discretization. As a result, our simulations are less accurate in capturing interface kinetics along the air–ice and air–water interfaces. However, considering the phase change kinetics involving the air phase is slow compared to the solidification/melting processes along the water–ice interface, we suspect the overall error on *wet* snow processes is small.

https://doi.org/10.1021/acs.cgd.4c00539
Cryst. Growth Des. 2024, 24, 7808–7821

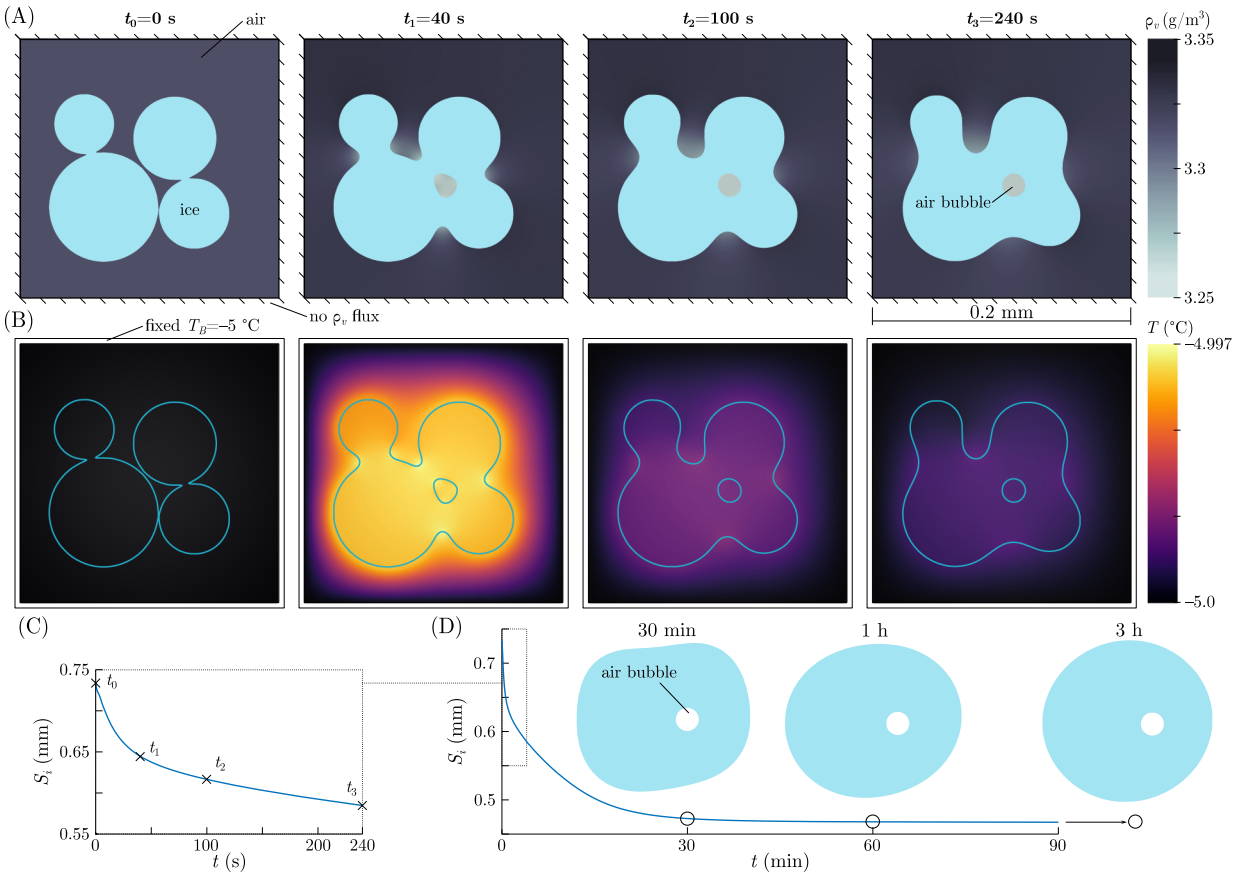

Figure 3. Dry snow metamorphism. Time evolution of (A) ice geometry and vapor concentration and (B) temperature distribution at t_0 = 0 s, t_1 = 40 s, t_2 = 100 s, and t_3 = 240 s. The blue solid line in (B) is the isoline ϕ_i = 0.5. Time evolution of the total ice perimeter S_i for short (C) and long (D) times. The ice geometry at t = 30 min, 1 h, and 3 h is included in (D).

3.3. Numerical Methods. We performed both 1D and 2D simulations of our model equations using the finite element method. In particular, we use a uniform mesh composed of bilinear (linear in 1D) basis functions. For the time integration, we use a semi-implicit algorithm based on the generalized-α method,[64,65] where we treat implicitly all the terms except the function M_0 and the parameter ξ_T, which are constant during each time step. We use the Newton−Raphson method with an adaptive time-stepping scheme to solve the resulting nonlinear system. To avoid singularities and numerical issues, we regularize the functions ρ, c_p, K, and ρ_{SE} (see Section 2.5 in the Supporting Information).

We impose no-flux boundary conditions for the phase variables and a Dirichlet boundary condition for the temperature. The vapor boundary condition is either Dirichlet or no-flux, depending on specific case studies. In most simulations, we initialize the vapor density with the saturated vapor density for ice at the prescribed temperature.

4. RESULTS

4.1. Directional Solidification and Nucleation of a Third Phase. In this section, we demonstrate the ability of our model to capture directional solidification as imposed by a temperature gradient and the nucleation of a third phase in a system that is initially composed of two phases only. In particular, we present three 1D simulations in Figure 2 that show (a) the complete freezing of water in an initial ice−water−air system (Figure 2A), (b) water nucleation in an initial ice−air system (Figure 2B), and (c) ice nucleation in an initial water−air system (Figure 2C). To perform these 1D simulations, we impose fixed temperatures and no-flux boundary conditions for the vapor phase on the two ends of the domain, which measures 1 mm in length and is discretized with 2000 elements.

In the freezing simulation (Figure 2A), the initially imposed temperature gradient results in the directional solidification of water toward the air phase. At each time step, the temperature distribution appears to be piecewise linear, which confirms the quasi-steady behavior of T as discussed in Section 3.1. Although the ρ_v dynamics are also quasi-steady, its distribution is not always linear (see t = 27 and 27.5 s in Figure 2A). This nonlinear response is primarily triggered when a new ice−air interface is established upon complete freezing (∼27.5 s), and a new equilibrium is established to satisfy the saturated vapor density in the presence of ice, prescribed by eq 8.

The nucleation simulations demonstrate significantly more nonlinear dynamics. In the water nucleation simulation (Figure 2B), we impose 0 and 6 °C on the left and right boundaries of the domain, respectively, to induce melting at the initial ice−air interface. In the ice nucleation simulation (Figure 2C), the water−air system is initially at −2 °C uniformly, and we consider the ice nucleation temperature T_{nucl} = −1 °C. Ice nucleation onsets, preferentially toward the water phase, well before the temperature on the water−air interface increases to T_{nucl} (Figure 2C, t = 0.2 s). At t = 0.3 s, when $T > T_{nucl}$ on the interface, the ice phase is fully developed. Both types of nucleation described here are highly energetic events, leading

https://doi.org/10.1021/acs.cgd.4c00539
Cryst. Growth Des. 2024, 24, 7808−7821

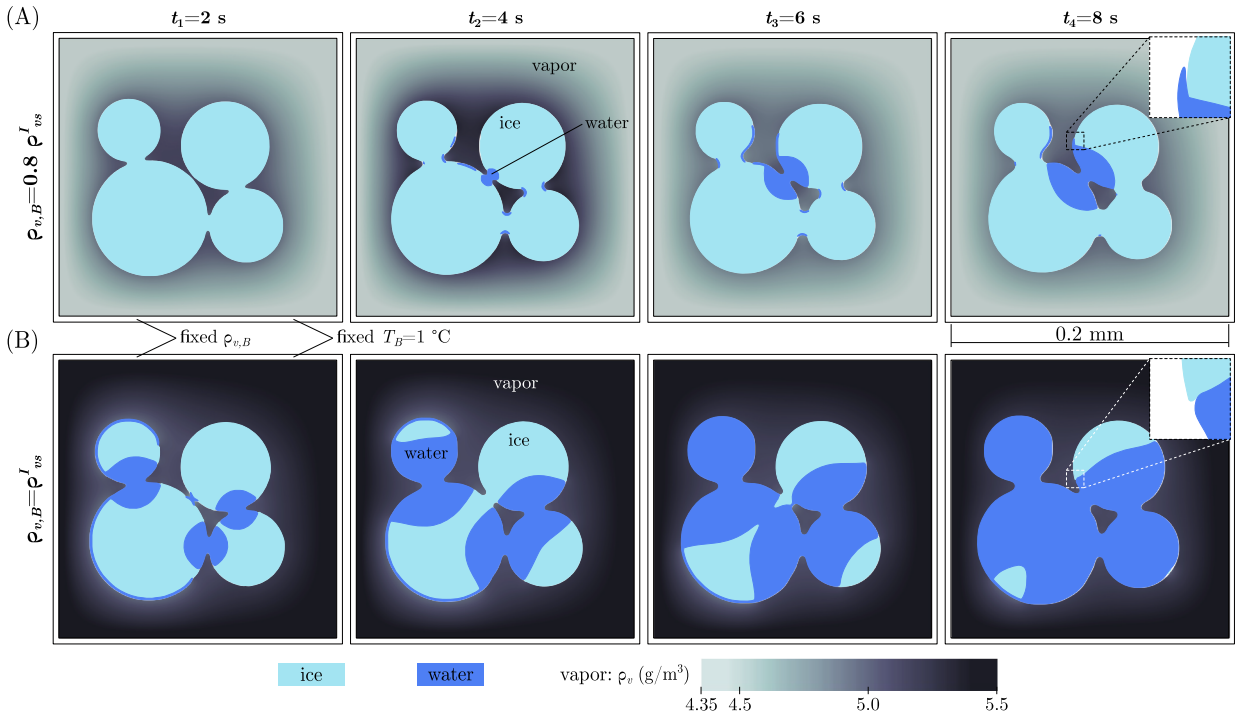

Figure 4. Impact of vapor concentration on melting of snow. Time evolution of the ice and water phases and vapor concentration for boundary vapor concentration of (A) $\rho_{v,B} = 0.8\rho^I_{vs}$ and (B) $\rho_{v,B} = \rho^I_{vs}$ when snow melts with $T_B = 1$ °C. The initial snow geometry is plotted in Figure 3. The insets show a zoom-in of the triple junction region. Note that the figure inset rendering is created by showing $\phi_i > 0.5$ as the ice phase in light blue, $\phi_w > 0.5$ as the water phase in dark blue, and $\phi_a > 0$ (equivalent to regions with $\phi_i < 0.5$ and $\phi_w < 0.5$) as the air phase in white.

to rapid changes in temperature and saturated vapor density in the nucleation region. As a result, the T and ρ_v profiles are no longer linear in contrast to the directional freezing problem (Figure 2A). We note that here nucleation only occurs at the phase−phase interface due to its mathematical formulation in eq 10.

We note that the phase-field variables maintain the tanh-profile (quasi-equilibrium profile) during the freezing simulation (insets of Figure 2A), but such profiles are temporarily lost during the nucleation simulations (insets of Figure 2B,C). In the latter cases, the loss of the tanh-profile is due to changes in mobility M_0 (eq 16) during the dynamic nucleation events and could result in small errors in curvature calculations and thus influence the kinetics of phase change through the Gibbs−Thomson condition. Nevertheless, the tanh-profile is recovered shortly after nucleation (e.g., at $t = 1$ s in Figure 2B,C); thus, the undesired loss of the tanh-profile is temporary (occurs only during nucleation), and for this reason, we assume that its impact on the overall kinetics of the problem is negligible.

4.2. Simulation of Dry Snow Metamorphism in 2D.

Under thermal conditions when the liquid water phase is absent ($\phi_w = 0$), our model reduces to the two-phase model for dry snow metamorphism first proposed in Kaempfer and Plapp:[34]

$$\frac{\partial \phi_i}{\partial t} = -3M_0\left(\frac{1}{\varepsilon}\phi_i(1-\phi_i)(1-2\phi_i) - \varepsilon\nabla^2\phi_i\right) + \alpha_{sub}\phi_i^2\phi_a^2\frac{\rho_v - \rho^I_{vs}(T)}{\rho_i} \quad (30)$$

$$\frac{1}{\xi_T}\rho(\bar{\phi})c_p(\bar{\phi})\frac{\partial T}{\partial t} = \nabla\cdot[K(\bar{\phi})\nabla T] - \rho(\bar{\phi})L_{sub}\frac{\partial \phi_a}{\partial t} \quad (31)$$

$$\frac{1}{\xi_v}\frac{\partial(\phi_a\rho_v)}{\partial t} = \nabla\cdot[\phi_a D_v(T)\nabla\rho_v] + \rho_{SE}\frac{\partial \phi_a}{\partial t} \quad (32)$$

with $\partial\phi_a/\partial t = -\partial\phi_i/\partial t$. Here, we show a 2D example of the dry metamorphism model using a simple snow geometry composed of four circular ice grains in contact (see t_0 in Figure 3A). The domain measures 0.2 × 0.2 mm^2 and is meshed with 400 × 400 elements. We impose a fixed temperature $T_B = -5$ °C and a no-flux of ρ_v on all boundaries of the domain. Over the 90 min time span of the simulation, we plot the time evolution of the ice phase ϕ_i and vapor concentration ρ_v (Figure 3A), along with the T (Figure 3B) and the total ice interface length S_i (Figure 3C,D). Also known as coarsening, dry snow metamorphism under isothermal conditions is a curvature-driven process, which minimizes the total interfacial length and the curvature of the system. The process penalizes regions of high curvature and is driven by vapor mass transfer between regions of different curvatures.[3] Our simulation readily illustrates the above mechanism. We observe that the ice grains quickly sinter (before $t_1 = 40$ s) and the coarsening process gradually slows down, as measured by the decay in slope in Figure 3C,D. Accompanying these geometric changes are the dynamics in T distribution due to latent heat generation in regions of higher curvature (see Figure 3B). The simulation also captures the entrapment of an air bubble during the coarsening process. At a steady state (e.g., $t = 3$ h in Figure 3D), the vapor concentration inside the bubble is set by its curvature according to the Gibbs−Thomson condition (eq 20).

https://doi.org/10.1021/acs.cgd.4c00539
Cryst. Growth Des. 2024, 24, 7808−7821

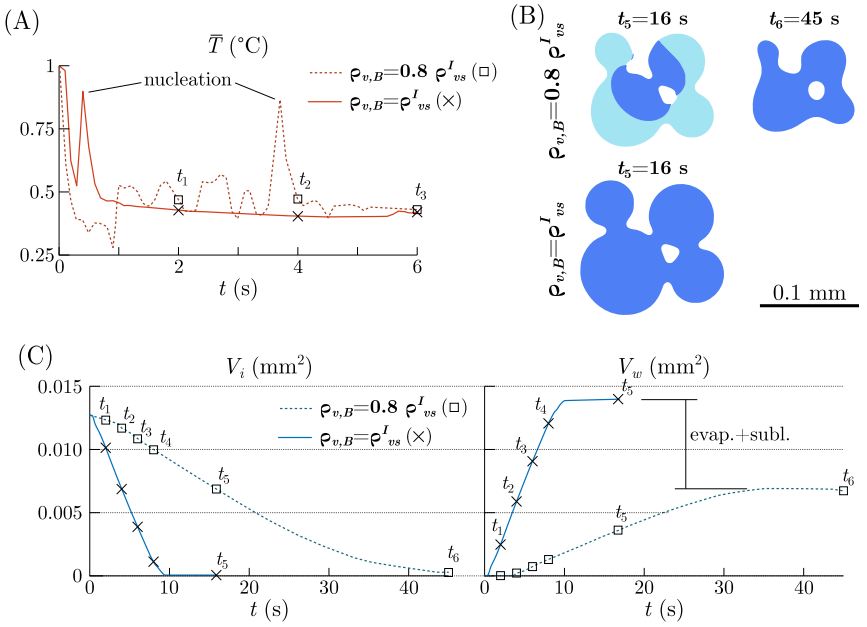

Figure 5. More detailed analysis of the simulations is shown in Figure 4. (A) Time evolution of the spatial-average temperature ($\overline{T}$) when $\rho_{v,B}$ = 0.8ρ^I_{vs} (dashed line) and $\rho_{v,B}$ = ρ^I_{vs} (solid line). (B) Ice and water phases at times t_5 = 16 s and t_6 = 45 s when $\rho_{v,B}$ = 0.8ρ^I_{vs} (top) and at time t_5 = 16 s when $\rho_{v,B}$ = ρ^I_{vs} (bottom). (C) Time evolution of the ice (V_i, left) and water (V_w, right) volume when $\rho_{v,B}$ = 0.8ρ^I_{vs} (dashed lines) and $\rho_{v,B}$ = ρ^I_{vs} (solid lines).

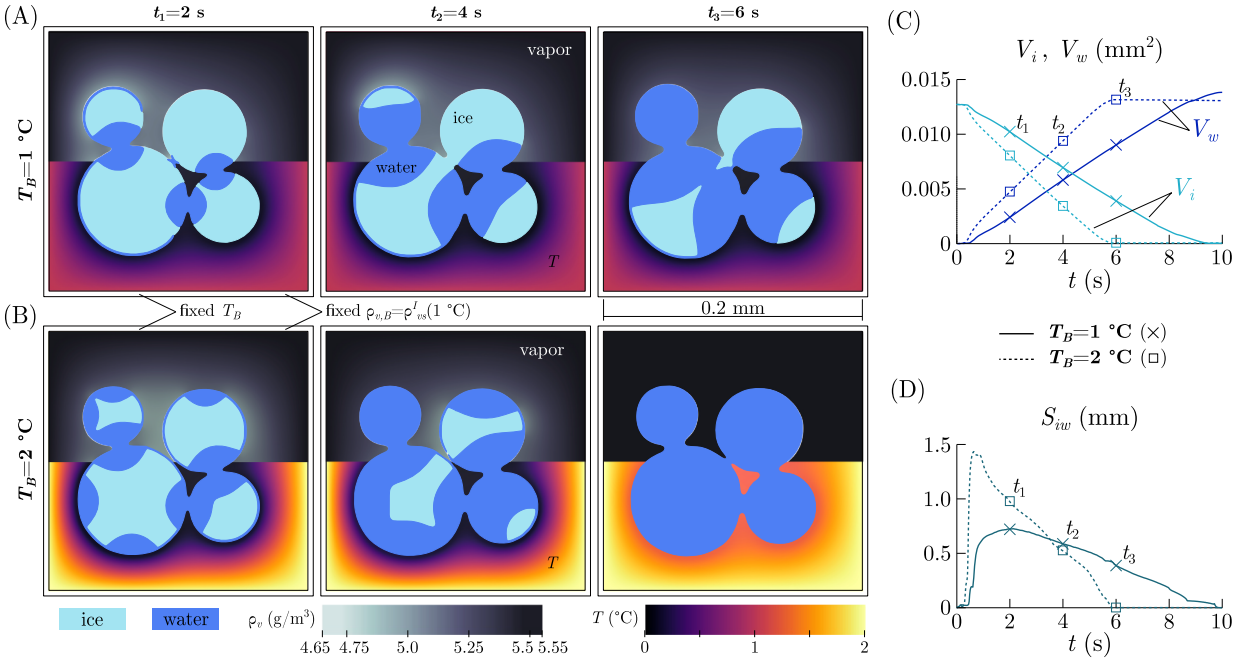

Figure 6. Impact of temperature on melting of snow. (A, B) Time evolution of the ice and water phases and vapor concentration (upper half of each panel) and temperature distribution (bottom half of each panel) for boundary temperatures (A) T_B = 1 °C and (B) T_B = 2 °C. The initial snow geometry is plotted in Figure 3. (C) Time evolution of the ice (V_i, light blue) and water (V_w, dark blue) volume for T_B = 1 °C (solid lines) and T_B = 2 °C (dashed lines). (D) Time evolution of ice−water interface length S_{iw} for T_B = 1 °C (solid line) and T_B = 2 °C (dashed line).

4.3. Simulations of Wet Snow Dynamics in 2D. In this section, we perform a suite of numerical simulations of our full model to investigate wet snow dynamics as it undergoes a phase transitions. Due to the high computational cost of the model, here we only focus on small-sized domains (∼mm) in 2D.

4.3.1. Influence of Vapor Concentration. In this part, we study the impact of the vapor concentration on the kinetics of melt generation when the initially dry material is subjected to melting. To achieve this, we consider the same four-grain geometry as the initial dry snow simulation in Figure 3, impose a boundary temperature of T_B = 1 °C, and run two simulations with different vapor concentrations on the boundary, denoted as $\rho_{v,B}$. In particular, we impose an undersaturated vapor density, $\rho_{v,B}$ = 0.8ρ^I_{vs}(1 °C), in the first simulation (Figure 4A)

https://doi.org/10.1021/acs.cgd.4c00539
Cryst. Growth Des. 2024, 24, 7808−7821

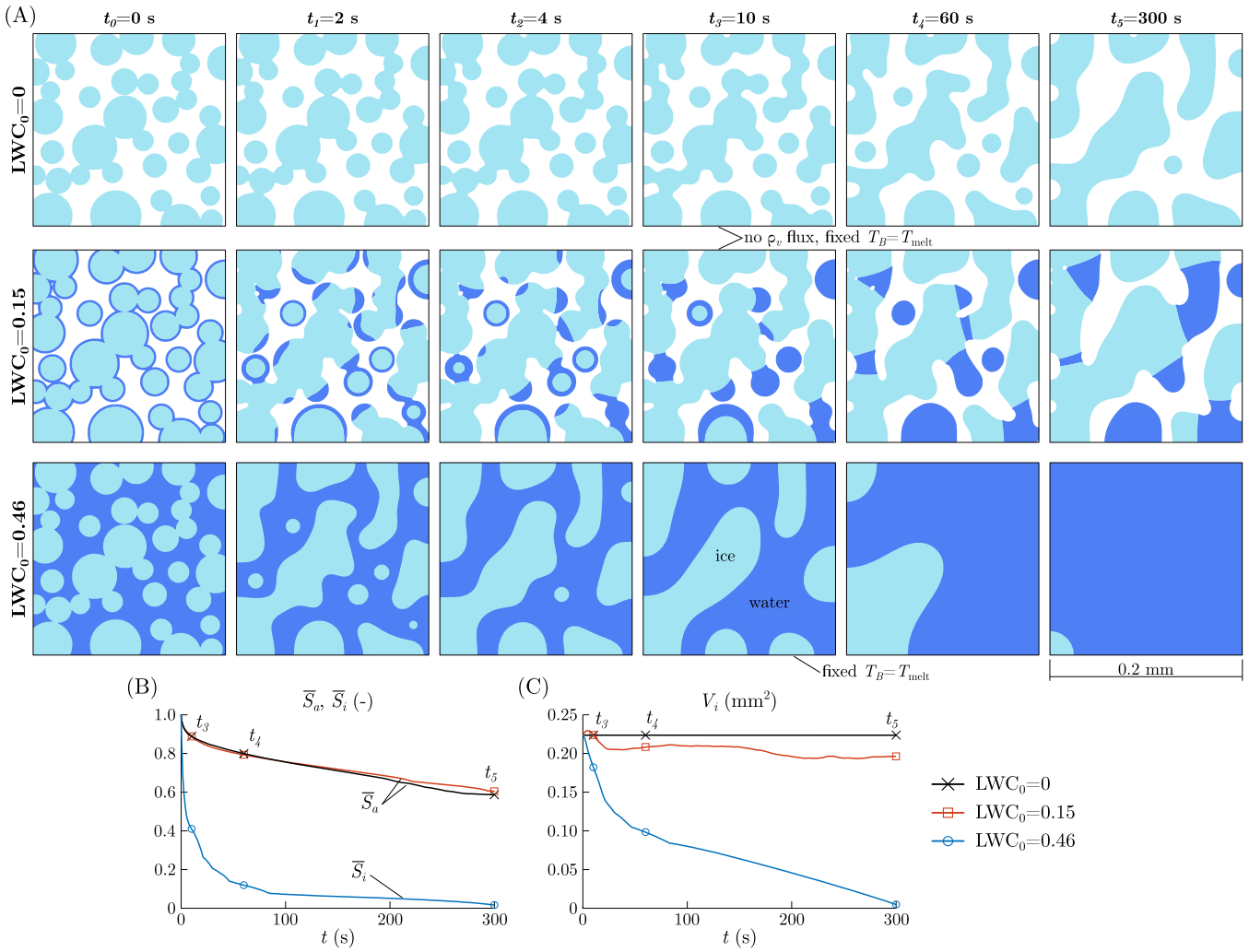

Figure 7. Influence of LWC on quasi-isothermal snow metamorphism, where boundary temperature T_B is fixed to T_{melt}. (A) Time evolution of the ice and water phases for the initial LWC (LWC$_0$) of 0 (top row), 0.15 (center row), and 0.46 (bottom row; fully wet). (B) Time evolution of the normalized interface length of the air phase ($\overline{S}_a$) for LWC$_0$ = 0 (black) and LWC$_0$ = 0.15 (red) and of the ice phase ($\overline{S}_i$) for LWC$_0$ = 0.46 (blue). The interface length is normalized by its initial value. (C) Time evolution of the ice volume (V_i) for LWC$_0$ = 0 (black), 0.15 (red), and 0.46 (blue).

and a saturated vapor density, $\rho_{v,B} = \rho^I_{vs}(1\ °C)$, in the second one (Figure 4B).

We quantify these two simulations by plotting the time evolution of the spatially averaged temperature $\overline{T}$, volume of ice phase V_i, and water phase V_w in Figure 5A,C. The results illustrate that, when the initial vapor phase is undersaturated, melt nucleation is delayed and the kinetics of melt generation is slower (Figure 5C). We explain this from the perspective of thermal balance. Because both sublimation and melt generation require energy input, an unsaturated vapor phase will reduce the amount of energy available for melting. This is evident when we observe that the average temperature decrease is stronger in the unsaturated vapor case (Figure 5A, dashed line). This lower temperature also causes a delay in water nucleation (Figures 4A and 5C). We also compare the final snapshots of the two simulations, taken at different times (t = 45 s for the first and t = 16 s for the second simulation), but both correspond to a state when ice no longer exists (Figure 5B). It is evident that there is significantly less meltwater in the first simulation, which is caused by the significant sublimation that claims part of the ice in order to saturate the vapor phase.

Finally, we want to remark that while water nucleation occurs in many parts of the ice interface, melting into the ice phase advances only in some regions of the interface because the process is limited by the thermal energy influx (Figures 4 and 5). In particular, we observe that melting usually starts at the grain contact regions because larger curvatures induce higher temperatures, as is already shown in the case of dry snow (Figure 3B).

4.3.2. Influence of Temperature. In this part, we study the impact of the temperature on wet snow evolution. Using the same initial dry snow geometry (Figure 3), here we fix the vapor concentration on the boundary such that $\rho_{v,B} = \rho^I_{vs}(1\ °C)$ and consider two different boundary temperature T_B's, namely, T_B = 1 °C (Figure 6A) and T_B = 2 °C (Figure 6B). We further quantify these two simulations with the time evolution of V_i and V_w (Figure 6C) and the ice−water interface length S_{iw} (Figure 6D). As expected, we observed that melting is faster at a higher boundary temperature (Figure 6C). In particular, our results illustrate that a higher temperature accelerates melting by promoting melt nucleation and thus increases the amount of the ice−water interface available for melt advancing (Figure 6D). In particular, we observe that a film of nucleated

https://doi.org/10.1021/acs.cgd.4c00539
Cryst. Growth Des. 2024, 24, 7808−7821

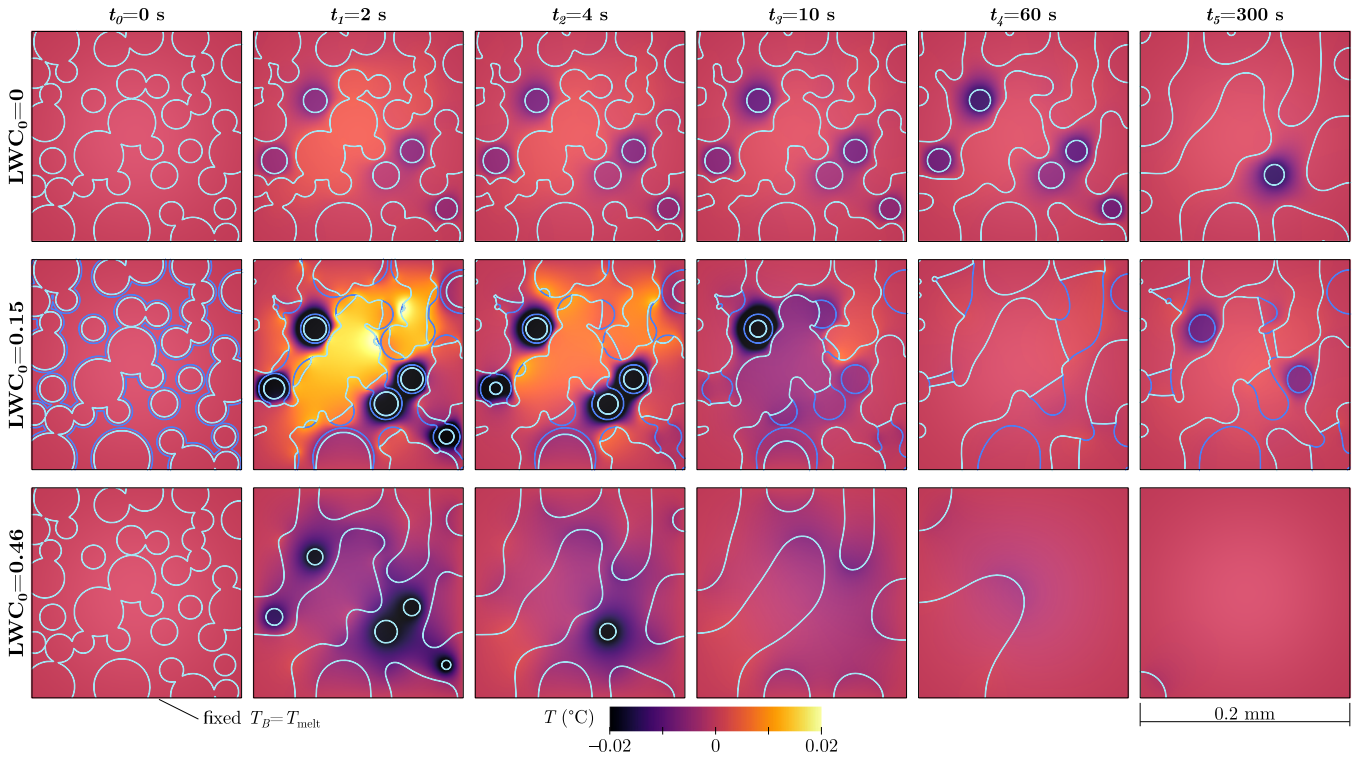

Figure 8. Influence of LWC on quasi-isothermal snow metamorphism, where boundary temperature T_B is fixed to T_{melt}. Time evolution of the temperature distribution for initial LWC (LWC$_0$) was 0 (top row), 0.15 (center row), and 0.46 (bottom row; fully wet). Light and dark blue lines represent the ice and water interfaces, respectively.

water completely surrounds the ice phase at the higher temperature (Figure 6B), while the water film only appears in some regions of the ice interface at the lower temperature (Figure 6A). After nucleation, we observe that melting advances only in the three grain contact locations for low T_B, while melting progresses in a few more locations, some away from grain contacts, at high T_B (Figure 6B).

Finally, upon complete melting, the two simulations display a small difference in V_w (Figure 6C, at t = 10 s). This difference is caused by the imposed T and ρ_v boundary conditions. Since we impose $\rho_{v,B} = \rho^I_{vs}(1\ °C)$ for both simulations, vapor concentration on the boundary is out of equilibrium for the case of T_B = 2 °C. This induces a vapor outflux through the boundary, which is reflected in the final value of V_w via sublimation/evaporation.

4.3.3. Influence of Liquid Water Content. In this section, we study the influence of the LWC on wet snow metamorphism. We consider a simplified snow geometry composed of circular ice grains in a domain of 0.2 × 0.2 mm^2 meshed with 800 × 800 elements (Figure 7A, t = 0 s). We run three simulations with different initial LWC (LWC$_0$) that correspond to dry (LWC$_0$ = 0), partially wet (LWC$_0$ = 0.15), and fully wet (LWC$_0$ = 0.46) snow. The initial ice phase distribution is the same for all three cases. For the partially wet snow, we impose a water film of 2.6 μm thickness uniformly surrounding the ice grains. For fully wet snow, we fill the pore space entirely with the liquid phase. We adopt the parameter value $\varepsilon = 2 \times 10^{-7}$ m. To keep the system under quasi-isothermal conditions, we impose a fixed temperature $T_B = T_{melt}$ and no-flux in terms of vapor density ρ_v on all boundaries.

The simulation results (Figures 7 and 8) illustrate the influence of LWC$_0$ on the detailed dynamics of metamorphism. In particular, when comparing against dry snow, we find that partially wet snow evolves toward larger and fewer ice clusters faster (e.g., LWC$_0$ = 0 and LWC$_0$ = 0.15 at t = 10 s in Figure 7A). While this accelerated coarsening in partially wet snow is visually apparent, a plot of the normalized interface length $\overline{S}_a$ does not readily capture this difference (Figure 7B, black and red lines). Note that $\overline{S}_a$ in the partially wet snow accounts for the interface of the combined phase of ice and water ($\phi_i + \phi_w$). Meanwhile, the coarsening speed of the fully wet snow is much faster, as captured visually in Figure 7A and also in terms of the normalized ice interface length, $\overline{S}_i$ (Figure 7B, blue line).

Wet snow also experiences a broader range of dynamic temperatures than dry snow during metamorphism (Figure 8). This may be explained by the fact that in wet snow, the thermal fluctuations are dominated by the latent heat released/absorbed during the freezing/melting process, which is orders of magnitude faster than the process of deposition/sublimation in dry snow (see Table S1 in the Supporting Information). The temperature distribution also reflects the Gibbs−Thomson effect: because the equilibrium temperature (T^{equil}, eq 19) decreases with increasing ice grain curvature, smaller ice grains require colder temperature ($T^{equil} < T_{melt}$) to be stable (Figure 8). Because we impose a temperature T_{melt} at the boundaries, which is higher than the equilibrium temperature for curved grains, we find that all ice grains eventually melt away in the case of fully saturated snow (Figure 7A,C and LWC = 0.46). Note that here if we initialize the simulation with *concave* grain shapes, this will lead to $T^{equil} > T_{melt}$ and complete freezing of the water in the case of fully wet snow.

A key characteristic of dry snow metamorphism is the reduction in the microstructure surface area while maintaining an almost constant ice volume (Figure 7B−C, black curves). Interestingly, we find that for the partially wet snow case

https://doi.org/10.1021/acs.cgd.4c00539
Cryst. Growth Des. 2024, 24, 7808−7821

investigated here, the volume of the air phase is also roughly constant throughout the simulation (not shown here). We attribute this to the fact that the water storage capacity of the air is limited (the initial vapor concentration is already close to the saturated vapor density). Nevertheless, we do observe a small mass exchange between the ice and water phases for partially wet snow, as evidenced by the changes in V_i for $LWC_0 = 0.15$ in Figure 7C.

5. NUMERICAL CHALLENGES AND MODEL IMPROVEMENTS

We have so far presented a series of 1D and 2D simulations of wet snow in domains of limited sizes (~0.2 mm). The reason we do not explore larger problems in 3D is the high computational cost associated with these simulations. This limits our ability to compare with experimental studies, which are always in 3D and done on samples that are ~ cm in size (e.g., in Colbeck[5]). Here, we summarize these computational challenges, as well as points for model improvements in future work.

In order to accurately capture the kinetics defined by the Gibbs−Thomson conditions, our model requires that the numerical interface width parameter $\varepsilon < 10^{-8}$ m (see Section 3.2). The consequence of this requirement is the need for a rather fine numerical mesh that resolves such an interface, making it computationally expensive to simulate larger problems. An adaptive mesh refinement algorithm, rather than the uniform mesh used in this work, would allow one to run millimeter- and centimeter-scale simulations in reasonable computational times. Additionally, mathematical additions to our model based on an asymptotic analysis for the thermal problem with asymmetric diffusivities could further improve the robustness of our model at the interface.

Another cause of high computational cost is the need to resolve the kinetics of different processes. In this work, we resort to a monolithic scheme in which our time step size is limited by the fastest process. We have alleviated this issue partially using the time-scaling strategy explained in Section 3.1. Another way to speed up time integration is to neglect the phase transitions related to the vapor phase during melting/freezing scenarios. The errors introduced with this approach would be small as long as melting/freezing occurs for short time intervals compared with the total time of interest.

Finally, our model is currently not suited for studying the *dynamics* of the triple junction—the region where the air, liquid, and ice phases contact—when the system is near the triple point. At the triple point, defined here as $\{T, \rho_v\} = \{T_{melt}, \rho_{vs}^{I}(T_{melt})\}$, the triple junction is expected to display an equilibrium configuration defined by the surface tensions in eq 6. In our model, an initial nonequilibrium triple junction configuration will evolve toward equilibrium through the comovement of the water−air, air−ice, and water−ice interfaces. However, because each interface moves at different speeds, as defined by the phase-dependent mobility (eq 16), a true equilibrium may not be possible. Instead, the model produces oscillations around the triple junction that impede the achievement of the equilibrium configuration.[59,60] Far away from the triple point, phase change kinetics around the triple junction dominate over the surface tension kinetics, and these oscillations do not appear.

For future work, we will focus on a more realistic representation of the nucleation process that includes randomized Gaussian noise,[66,67] which would produce a more realistic behavior of the wet snow metamorphism problem. The current model also does not consider the density difference between the solid ice and liquid water phases, which would introduce a small mass conservation error (the model is volume conserved). Our model might be expanded based on Hagiwara et al.,[26] Zhang et al.,[27] and Huang et al.[68] to account for mass conservation during melting/freezing, but further research is needed.

6. CONCLUSIONS

We propose a nonvariational phase-field model for wet snow metamorphism. The model accounts for the ice, water, and air phases, along with the temperature and vapor dynamics, and captures the actual kinetics of solidification, sublimation, and evaporation (and the opposite transitions). To the best of our knowledge, this is the first phase-field model that simultaneously reproduces the different phase transitions of water. The model results unveil the intimate coupling among the various transport and phase change processes involved in wet snow metamorphism. Our results show that local humidity conditions affect snow melting and melt refreezing. The results also reveal the differences between dry and wet snow metamorphism when water flow is not considered: partially and fully wet snow experience larger thermal fluctuations due to the dominant freeze/melt processes, and the coarsening rate is higher for fully wet snow compared to dry snow as expected. However, our observations are based on numerically generated partial wet snow, where a liquid film of constant thickness is imposed over all ice grain surfaces. We recognize that this way of initializing the simulation may not represent actual liquid film distribution in wet snow and thus may result in unrealistic dynamics. In addition, because we do not consider thin film flow and other capillary-driven processes of the liquid phase, our model may be missing key fluid mechanical processes that influence how wet snow evolves.

The current results focus on 1D and 2D problems due to the high computational cost of the model equations. Future modification, extension, and application of this model in 3D may be used to quantitatively analyze the evolution of the snow pore structure during wet snow metamorphism, which dictates the thermo-mechanical and hydraulic properties of the snow at larger scales. The proposed modeling framework has proven useful in studying wet snow metamorphism and may be the basis to investigate other mm- or cm-scale problems involving water phase transitions such as the freezing of a water droplet on a surface,[25,69−71] human-induced thermo-mechanical changes of icy planetary surfaces, or water spray cooling.

■ ASSOCIATED CONTENT

Supporting Information

The Supporting Information is available free of charge at https://pubs.acs.org/doi/10.1021/acs.cgd.4c00539.

Equivalence to models of two-phase transition and additional details for numerical implementation (PDF)

■ AUTHOR INFORMATION

Corresponding Authors

Adrian Moure − *Department of Mechanical and Civil Engineering, California Institute of Technology, Pasadena, California 91125-0002, United States*; Email: amoure@caltech.edu

https://doi.org/10.1021/acs.cgd.4c00539
Cryst. Growth Des. 2024, 24, 7808−7821

Xiaojing Fu − *Department of Mechanical and Civil Engineering, California Institute of Technology, Pasadena, California 91125-0002, United States;* orcid.org/0000-0001-7120-704X; Email: rubyfu@caltech.edu

Complete contact information is available at: https://pubs.acs.org/10.1021/acs.cgd.4c00539

Notes

The authors declare no competing financial interest.

■ ACKNOWLEDGMENTS

The authors acknowledge the partial support from the Resnick Sustainability Institute at California Institute of Technology, the National Science Foundation under Grant No. EAR-2243631, and the ACS Petroleum Research Fund Doctoral New Investigator Grant No. 66867-DNI9. The authors also acknowledge insightful discussions with Dr. Quirine Krol.

■ REFERENCES

(1) Colbeck, S. C. *Theory of metamorphism of wet snow*; U.S. Army Cold Regions Research and Engineering Laboratory, 1973.
(2) Colbeck, S. C. In The basic ideas behind snow metamorphism, Proceedings of the International Snow Science Workshop, 1996.
(3) Colbeck, S. C. Thermodynamics of snow metamorphism due to variations in curvature. *Journal of Glaciology* **1980**, *26*, 291−301.
(4) Colbeck, S. C. An overview of seasonal snow metamorphism. *Reviews of Geophysics* **1982**, *20*, 45−61.
(5) Colbeck, S. C. Statistics of coarsening in water-saturated snow. *Acta Metall.* **1986**, *34*, 347−352.
(6) Colbeck, S. C. *A Review of Sintering in Seasonal Snow*; U.S. Army Cold Regions Research and Engineering Laboratory, 1997.
(7) Raymond, C. F.; Tusima, K. Grain coarsening of water-saturated snow. *Journal of Glaciology* **1979**, *22*, 83−105.
(8) Wakahama, G. The role of meltwater in densification processes of snow and firn. *Int. Assoc. Hydrol. Sci. Publ.* **1975**, *114*, 66−72.
(9) Gundlach, B.; Ratte, J.; Blum, J.; Oesert, J.; Gorb, S. Sintering and sublimation of micrometre-sized water-ice particles: The formation of surface crusts on icy Solar System bodies. *Mon. Not. R. Astron. Soc.* **2018**, *479*, 5272−5287.
(10) Johnson, C. A. Generalization of the Gibbs-Thomson equation. *Surf. Sci.* **1965**, *3*, 429−444.
(11) Löwe, H.; Spiegel, J.; Schneebeli, M. Interfacial and structural relaxations of snow under isothermal conditions. *Journal of Glaciology* **2011**, *57*, 499−510.
(12) Kaempfer, T. U.; Schneebeli, M. Observation of isothermal metamorphism of new snow and interpretation as a sintering process. *J. Geophys. Res.: Atmos.* **2007**, *112*, .
(13) Pinzer, B.; Schneebeli, M.; Kaempfer, T. Vapor flux and recrystallization during dry snow metamorphism under a steady temperature gradient as observed by time-lapse micro-tomography. *Cryosphere* **2012**, *6*, 1141−1155.
(14) Wang, X.; Baker, I. Evolution of the specific surface area of snow during high-temperature gradient metamorphism. *J. Geophys. Res.: Atmos.* **2014**, *119*, 690−703.
(15) Fife, J.; Gibbs, J.; Gulsoy, E.; Park, C.-L.; Thornton, K.; Voorhees, P. The dynamics of interfaces during coarsening in solid−liquid systems. *Acta Mater.* **2014**, *70*, 66−78.
(16) Krol, Q.; Löwe, H. Analysis of local ice crystal growth in snow. *Journal of Glaciology* **2016**, *62*, 378−390.
(17) Legagneux, L.; Domine, F. A mean field model of the decrease of the specific surface area of dry snow during isothermal metamorphism. *J. Geophys. Res.: Earth Surf.* **2005**, *110*, .
(18) Krol, Q.; Löwe, H. Upscaling ice crystal growth dynamics in snow: Rigorous modeling and comparison to 4D X-ray tomography data. *Acta Mater.* **2018**, *151*, 478−487.
(19) Brun, E. Investigation on wet-snow metamorphism in respect of liquid-water content. *Annals of Glaciology* **1989**, *13*, 22−26.
(20) Ebner, P. P.; Coulin, A.; Borner, J.; Wolfsperger, F.; Hohl, M.; Schneebeli, M. Liquid-water content and water distribution of wet snow using electrical monitoring. *Cryosphere* **2020**, *2020*, 1−34.
(21) Stein, J.; Laberge, G.; Lévesque, D. Monitoring the dry density and the liquid water content of snow using time domain reflectometry (TDR). *Cold Regions Science and Technology* **1997**, *25*, 123−136.
(22) Coléou, C.; Lesaffre, B. Irreducible water saturation in snow: experimental results in a cold laboratory. *Annals of glaciology* **1998**, *26*, 64−68.
(23) Brun, E.; David, P.; Sudul, M.; Brunot, G. A numerical model to simulate snow-cover stratigraphy for operational avalanche forecasting. *Journal of Glaciology* **1992**, *38*, 13−22.
(24) Donahue, C.; Skiles, S. M.; Hammonds, K. Mapping liquid water content in snow at the millimeter scale: an intercomparison of mixed-phase optical property models using hyperspectral imaging and in situ measurements. *Cryosphere* **2022**, *16*, 43−59.
(25) Sebilleau, J.; Ablonet, E.; Tordjeman, P.; Legendre, D. Air humidity effects on water-drop icing. *Phys. Rev. E* **2021**, *104*, No. L032802.
(26) Hagiwara, Y.; Ishikawa, S.; Kimura, R.; Toyohara, K. Ice growth and interface oscillation of water droplets impinged on a cooling surface. *J. Cryst. Growth* **2017**, *468*, 46−53.
(27) Zhang, W.; Shahmardi, A.; Choi, K.-S.; Tammisola, O.; Brandt, L.; Mao, X. A phase-field method for three-phase flows with icing. *J. Comput. Phys.* **2022**, *458*, No. 111104.
(28) Vahab, M.; Pei, C.; Hussaini, M. Y.; Sussman, M.; Lian, Y. In An adaptive coupled level set and moment-of-fluid method for simulating droplet impact and solidification on solid surfaces with application to aircraft icing, 54th AIAA Aerospace Sciences Meeting, 2016; p 1340.
(29) Vahab, M.; Murphy, D.; Shoele, K. Fluid dynamics of frozen precipitation at the air−water interface. *J. Fluid Mech.* **2022**, *933*, A36.
(30) Cristini, V.; Lowengrub, J. Three-dimensional crystal growth—II: nonlinear simulation and control of the Mullins−Sekerka instability. *J. Cryst. Growth* **2004**, *266*, 552−567.
(31) Wang, S.-L.; Sekerka, R.; Wheeler, A.; Murray, B.; Coriell, S.; Braun, R.; McFadden, G. Thermodynamically-consistent phase-field models for solidification. *Physica D: Nonlinear Phenomena* **1993**, *69*, 189−200.
(32) Karma, A.; Rappel, W.-J. Phase-field method for computationally efficient modeling of solidification with arbitrary interface kinetics. *Phys. Rev. E* **1996**, *53*, R3017.
(33) Bouvet, L.; Calonne, N.; Flin, F.; Geindreau, C. Snow Equi-Temperature Metamorphism Described by a Phase-Field Model Applicable on Micro-Tomographic Images: Prediction of Microstructural and Transport Properties. *J. Adv. Model. Earth Syst.* **2022**, *14*, No. e2022MS002998.
(34) Kaempfer, T. U.; Plapp, M. Phase-field modeling of dry snow metamorphism. *Phys. Rev. E* **2009**, *79*, No. 031502.
(35) Reitzle, M.; Ruberto, S.; Stierle, R.; Gross, J.; Janzen, T.; Weigand, B. Direct numerical simulation of sublimating ice particles. *International Journal of Thermal Sciences* **2019**, *145*, No. 105953.
(36) Fei, L.; Qin, F.; Wang, G.; Luo, K. H.; Derome, D.; Carmeliet, J. Droplet evaporation in finite-size systems: Theoretical analysis and mesoscopic modeling. *Phys. Rev. E* **2022**, *105*, No. 025101.
(37) Schweigler, K.; Said, M. B.; Seifritz, S.; Selzer, M.; Nestler, B. Experimental and numerical investigation of drop evaporation depending on the shape of the liquid/gas interface. *Int. J. Heat Mass Transfer* **2017**, *105*, 655−663.
(38) Ronsin, O. J.; Jang, D.; Egelhaaf, H.-J.; Brabec, C. J.; Harting, J. A phase-field model for the evaporation of thin film mixtures. *Phys. Chem. Chem. Phys.* **2020**, *22*, 6638−6652.
(39) Wang, Z.; Zheng, X.; Chryssostomidis, C.; Karniadakis, G. E. A phase-field method for boiling heat transfer. *J. Comput. Phys.* **2021**, *435*, No. 110239.

(40) Fu, X.; Cueto-Felgueroso, L.; Juanes, R. Thermodynamic coarsening arrested by viscous fingering in partially miscible binary mixtures. *Phys. Rev. E* **2016**, *94*, No. 033111.
(41) Shimizu, R.; Tanaka, H. Impact of complex topology of porous media on phase separation of binary mixtures. *Sci. Adv.* **2017**, *3*, No. eaap9570.
(42) Mao, S.; Kuldinow, D.; Haataja, M. P.; Košmrlj, A. Phase behavior and morphology of multicomponent liquid mixtures. *Soft Matter* **2019**, *15*, 1297−1311.
(43) Bhopalam, S. R.; Bueno, J.; Gomez, H. Elasto-capillary fluid−structure interaction with compound droplets. *Computer Methods in Applied Mechanics and Engineering* **2022**, *400*, No. 115507.
(44) Yue, P. Thermodynamically consistent phase-field modelling of contact angle hysteresis. *J. Fluid Mech.* **2020**, *899*, A15.
(45) Fu, X.; Cueto-Felgueroso, L.; Juanes, R. Viscous fingering with partially miscible fluids. *Physical Review Fluids* **2017**, *2*, No. 104001.
(46) Cueto-Felgueroso, L.; Fu, X.; Juanes, R. Pore-scale modeling of phase change in porous media. *Physical Review Fluids* **2018**, *3*, No. 084302.
(47) Fu, X.; Cueto-Felgueroso, L.; Juanes, R. Nonequilibrium Thermodynamics of Hydrate Growth on a Gas-Liquid Interface. *Phys. Rev. Lett.* **2018**, *120*, No. 144501.
(48) Fu, X.; Jimenez-Martinez, J.; Nguyen, T. P.; Carey, J. W.; Viswanathan, H.; Cueto-Felgueroso, L.; Juanes, R. Crustal fingering facilitates free-gas methane migration through the hydrate stability zone. *Proc. Natl. Acad. Sci. U. S. A.* **2020**, *117*, 31660−31664.
(49) Zhang, J.; Yuan, J.; Yuan, H. Numerical and experimental investigation of phase change characteristics and desalination effect of seawater freezing desalination in narrow channels. *Desalination* **2022**, *544*, No. 116145.
(50) Gomez, H.; Bures, M.; Moure, A. A review on computational modelling of phase-transition problems. *Philosophical Transactions of the Royal Society A* **2019**, *377*, No. 20180203.
(51) Boyer, F.; Lapuerta, C. Study of a three component Cahn-Hilliard flow model. *ESAIM: Mathematical Modelling and Numerical Analysis-Modélisation Mathématique et Analyse Numérique* **2006**, *40*, 653−687.
(52) Steinbach, I. Phase-field models in materials science. *Modell. Simul. Mater. Sci. Eng.* **2009**, *17*, No. 073001.
(53) Folch, R.; Plapp, M. Quantitative phase-field modeling of two-phase growth. *Phys. Rev. E* **2005**, *72*, No. 011602.
(54) Tóth, G. I.; Pusztai, T.; Gránásy, L. Consistent multiphase-field theory for interface driven multidomain dynamics. *Phys. Rev. B* **2015**, *92*, No. 184105.
(55) Allen, S. M.; Cahn, J. W. A microscopic theory for antiphase boundary motion and its application to antiphase domain coarsening. *Acta Metall.* **1979**, *27*, 1085−1095.
(56) Flatau, P. J.; Walko, R. L.; Cotton, W. R. Polynomial fits to saturation vapor pressure. *Journal of Applied Meteorology* **1992**, *31*, 1507−1513.
(57) Wexler, A. Vapor pressure formulation for ice. *J. Res. Natl. Bur. Stand., Sect. A* **1977**, *81*, 5.
(58) Massman, W. A review of the molecular diffusivities of H2O, CO2, CH4, CO, O3, SO2, NH3, N2O, NO, and NO2 in air, O2 and N2 near STP. *Atmos. Environ.* **1998**, *32*, 1111−1127.
(59) Miyoshi, E.; Takaki, T. Validation of a novel higher-order multi-phase-field model for grain-growth simulations using anisotropic grain-boundary properties. *Comput. Mater. Sci.* **2016**, *112*, 44−51.
(60) Moelans, N. New phase-field model for polycrystalline systems with anisotropic grain boundary properties. *Materials & Design* **2022**, *217*, No. 110592.
(61) Karma, A.; Rappel, W.-J. Quantitative phase-field modeling of dendritic growth in two and three dimensions. *Phys. Rev. E* **1998**, *57*, 4323.
(62) Karma, A. Phase-Field formulation for quantitative modeling of alloy solidification. *Phys. Rev. Lett.* **2001**, *87*, No. 115701.
(63) Ohno, M.; Takaki, T.; Shibuta, Y. Variational formulation and numerical accuracy of a quantitative phase-field model for binary alloy solidification with two-sided diffusion. *Phys. Rev. E* **2016**, *93*, No. 012802.
(64) Chung, J.; Hulbert, G. A time integration algorithm for structural dynamics with improved numerical dissipation: the generalized-α method. *J. Appl. Mech.* **1993**, *60*, 371−375.
(65) Jansen, K. E.; Whiting, C. H.; Hulbert, G. M. A generalized-α method for integrating the filtered Navier−Stokes equations with a stabilized finite element method. *Computer Methods in Applied Mechanics and Engineering* **2000**, *190*, 305−319.
(66) Karma, A.; Rappel, W.-J. Phase-field model of dendritic sidebranching with thermal noise. *Phys. Rev. E* **1999**, *60*, 3614.
(67) Cates, M.; Nardini, C. Classical Nucleation Theory for Active Fluid Phase Separation. *Phys. Rev. Lett.* **2023**, *130*, No. 098203.
(68) Huang, Z.; Lin, G.; Ardekani, A. M. A consistent and conservative Phase-Field model for thermo-gas-liquid-solid flows including liquid-solid phase change. *J. Comput. Phys.* **2022**, *449*, No. 110795.
(69) Snoeijer, J. H.; Brunet, P. Pointy ice-drops: How water freezes into a singular shape. *American Journal of Physics* **2012**, *80*, 764−771.
(70) Zeng, H.; Lyu, S.; Legendre, D.; Sun, C. Influence of gravity on the freezing dynamics of drops on a solid surface. *Physical Review Fluids* **2022**, *7*, No. 103605.
(71) Seguy, L.; Protière, S.; Huerre, A. Role of geometry and adhesion in droplet freezing dynamics. *Physical Review Fluids* **2023**, *8*, No. 033601.

https://doi.org/10.1021/acs.cgd.4c00539
Cryst. Growth Des. 2024, 24, 7808−7821